



CrossMark
click for updates

Cite this: *RSC Adv.*, 2014, 4, 64484

In situ synthesis of hierarchical In₂S₃–graphene nanocomposite photocatalyst for selective oxidation†

Xiuzhen Li,^{ab} Bo Weng,^{ab} Nan Zhang^{ab} and Yi-Jun Xu^{*ab}

We report a simple, *in situ* hydrothermal way to fabricate In₂S₃–graphene (GR) nanocomposites in which hierarchical In₂S₃ “petals” spread over the surface of GR sheets in virtue of the “structure directing” role of graphene oxide (GO) as the precursor of GR in a solution phase. With the addition of an appropriate amount of GO, the hierarchical petal-like In₂S₃ structures have been successfully grown on the two-dimensional (2D) GR “mat”. The as-synthesized In₂S₃–GR nanocomposites featuring good interfacial contact exhibit much higher photocatalytic activity toward selective oxidation of alcohols under visible light irradiation than blank In₂S₃. A series of characterization results disclose that the significantly enhanced photocatalytic performance of In₂S₃–GR nanocomposites can be ascribed to the integrative effect of the increased separation and transfer efficiency of photogenerated electron–hole pairs and the larger surface area. This work highlights the wide scope of fabricating GR-based semiconductor nanocomposites with specific architectural morphology by rationally utilizing the “structure directing” property of GO and extending their applications toward photocatalytic selective transformations.

Received 30th September 2014

Accepted 14th November 2014

DOI: 10.1039/c4ra13764g

www.rsc.org/advances

Introduction

In recent years, with the advance of two-dimensional (2D) graphene (GR) as an electrically conductive platform,¹ there has been increasing interest in designing GR–semiconductor composites as efficient photocatalysts for converting solar energy into chemical energy.^{2–10} Through taking advantage of the brilliant physical and chemical properties of GR,^{11–16} diverse GR–semiconductor nanocomposites have been extensively reported to show enhanced photocatalytic performance toward a myriad of applications, including photodegradation of pollutants (dyes, volatile organic pollutant, and bacteria), hydrogen production from water splitting, and photocatalytic selective organic transformations.^{4,10,17–35}

Generally, the synthetic method for fabrication of GR–semiconductor nanocomposites can be summarized as two categories.^{9,12,34} One is the hard integration of GR with solid semiconductor components and the other is the soft integration of graphene oxide (GO), as the precursor of GR, with soluble semiconductor precursors.^{10,21} For the hard integration method, the GR–semiconductor composites are obtained by the simple integration of GR with solid semiconductor, and the interfacial contact is often poor.^{21,35,36} In contrast, for the soft integration method, the “structure directing” role of GO in an aqueous phase can be readily utilized, which could promote the *in situ* anchoring of semiconductor particles onto the surface of reduced graphene oxide (RGO, also often called GR) mat in a solution phase. In this way, the as-obtained GR–semiconductor nanocomposites often have good interfacial contact, which is advantageous to the efficient separation of photogenerated charge carriers across the interfacial domain, thereby contributing to the enhanced photocatalytic performance of the GR–semiconductor nanocomposites.^{10,32,33}

Indium sulfide (In₂S₃), as one of the common studied semiconductors, is well crystallized into three polymorphic forms, including α -In₂S₃, β -In₂S₃ and γ -In₂S₃. Among these three forms, β -In₂S₃ with a narrow band gap, has been widely used as a kind of potential photocatalyst under visible light irradiation due to its excellent photosensitivity, photoconductivity, stable chemical and physical properties, and low toxicity.^{37–42} Thus far, in order to make better use of the properties for β -In₂S₃ in photocatalysis, much effort has been devoted to constructing In₂S₃ based materials with different

^aState Key Laboratory of Photocatalysis on Energy and Environment, College of Chemistry, Fuzhou University, Fuzhou, 350002, P. R. China

^bCollege of Chemistry, Fuzhou University, New Campus, Fuzhou, 350108, P. R. China. E-mail: yjxu@fzu.edu.cn; Tel: +86 591 83779326

† Electronic supplementary information (ESI) available: Experimental section for preparation of graphene oxide; the chemical structure of L-cysteine; the Fourier transformed infrared spectra (FTIR) of In₂S₃–1%GR and the original GO; the plot of transformed Kubelka–Munk function versus the energy of light for blank In₂S₃ and In₂S₃–GR nanocomposites with different weight addition ratios of GR; remaining fraction of various alcohols after the adsorption–desorption equilibrium is achieved over blank In₂S₃ and In₂S₃–1%GR; ESR spectra of radical adduct trapped by DMPO (DMPO–O₂^{•−}) over In₂S₃–1%GR suspension in the BTF solution without or with the visible light irradiation; summary of BET surface area and pore volume of blank In₂S₃ and In₂S₃–1%GR. See DOI: 10.1039/c4ra13764g

morphologies,^{37,38,43,44} such as one-dimensional (1D) In₂S₃ nanotubes and nanorods,^{37,45} 2D In₂S₃ nanoplates and nanosheets,^{41,46} three-dimensional (3D) flowerlike In₂S₃ and hierarchical architectures.^{38,40,47} Among them, hierarchical architectures, with modified structural, optical, and surface properties, are potentially useful for the application of photocatalysis.^{48,49}

Herein, we report a facile, *in situ* wet chemistry way to fabricate hierarchical In₂S₃-GR nanocomposites to boost the photoactivity of 3D In₂S₃. To the best of our knowledge, this is the first report on the application of In₂S₃-GR nanocomposites as visible light-driven photocatalyst for selective oxidation process. The higher photoactivity achieved on In₂S₃-GR than blank In₂S₃ toward selective oxidation of alcohols under visible light is mainly ascribed to the enhanced photogenerated electron-hole pairs separation and transfer as well as the larger surface area, resulting from the hierarchical architectures which are oriented by the "structure directing" role of GO. It is hoped that this work could provide useful information for careful design of GR-semiconductor nanocomposites with controllable architectures by making better use of the "structure directing" property of GO and extending their applications toward various photocatalytic selective transformations.

Experimental section

Materials

Indium(III) nitrate hydrate (In(NO₃)₃·4.5H₂O), L-cysteine (C₃H₇NO₂S), graphite powder, sulfuric acid (H₂SO₄), nitric acid (HNO₃), hydrochloric acid (HCl), sodium hydroxide (NaOH), potassium persulfate (K₂S₂O₈), phosphorus pentoxide (P₂O₅), potassium permanganate (KMnO₄), hydrogen peroxide 30% (H₂O₂), ethanol (C₂H₆O), benzyl alcohol (C₇H₈O), ammonium oxalate (N₂H₈C₂O₄, AO), benzoquinone (C₆H₄O₂, BQ), and *tert*-butyl alcohol (C₄H₁₀O, TBA) were supplied by Sinopharm chemical reagent Co., Ltd. (Shanghai, China). Benzotrifluoride (C₇H₅F₃, BTF), 4-methylbenzyl alcohol (C₈H₁₀O), 4-methoxybenzyl alcohol (C₈H₁₀O₂), 4-nitrobenzyl alcohol (C₇H₇NO₃), 4-chlorobenzyl alcohol (C₇H₇OCl), 4-fluorobenzyl alcohol (C₇H₇OF), cinnamyl alcohol (C₉H₁₀O), and 3-methyl-2-buten-1-ol (C₅H₁₀O) were purchased from Alfa Aesar Co., Ltd. (Tianjin, China). All the reagents were analytical grade and used without further purification. The deionized water was from local sources.

Synthesis

(a) Synthesis of graphene oxide (GO). GO was synthesized by a modified Hummers method,⁵⁰⁻⁵⁵ which was also expatiated in our previous works.^{21,33,56,57} The detail of the preparation procedure is presented in the ESI.†

(b) Fabrication of In₂S₃-GR nanocomposites with different weight addition ratios of GR. In a typical procedure, the given amount of as-prepared GO was ultrasonically dispersed in 40 mL distilled water and mixed with 0.5 mmol In(NO₃)₃·4.5H₂O. After stirring for 0.5 h, 2 mmol L-cysteine was added into the above mixture under vigorous stirring. After that, the pH was

adjusted to 8 by adding 1 M NaOH dropwise. After stirring for 1 h, the mixture was transferred into a 50 mL Teflon-lined stainless steel autoclave, which was sealed and treated at 180 °C for 16 h. Subsequently, the as-synthesized products were separated by centrifugation and washed with distilled water and absolute ethanol for three times and one time, respectively. After drying at 60 °C overnight, the target products were obtained.

(c) Preparation of blank flowerlike In₂S₃ structures. Blank flowerlike In₂S₃ structures were fabricated through the same procedure as above except for the addition of GO.

Characterization

The crystal-phase information of the samples was measured on a Bruker D8 Advance X-ray diffractometer with Cu K α radiation at 40 kV and 40 mA in the 2θ ranging from 10° to 80° with a scan rate of 0.02° s⁻¹. The UV-vis diffuse reflectance spectroscopy (DRS) was used to characterize the optical properties of the samples using UV-vis spectrophotometer (Cary 500, Varian) in which BaSO₄ was employed as a reference. Field-emission scanning electron microscopy (FESEM) was employed to detect the morphology of the samples on a FEI Nova NANOSEM 230 spectrophotometer. Transmission electron microscopy (TEM) images and high-resolution transmission electron microscopy (HRTEM) images were obtained using a JEOL model JEM 2010 EX instrument at an accelerating voltage of 200 kV. The Fourier transformed infrared spectroscopy (FTIR) was measured on a Nicolet Nexus 670 FTIR spectrophotometer at a resolution of 4 cm⁻¹. The photoluminescence (PL) spectra were obtained using an Edinburgh FL/FS900 spectrophotometer with an excitation wavelength of 420 nm. The nitrogen adsorption-desorption isotherms and Brunauer-Emmett-Teller (BET) specific surface areas were obtained on Micromeritics ASAP2010 equipment. The electron spin resonance (ESR) signal of the radicals spin-trapped by 5,5-dimethyl-1-pyrroline-*N*-oxide (DMPO) was measured on a Bruker EPR A300 spectrometer. The sample (5 mg) was dispersed in 0.5 mL purified benzotrifluoride into which 25 μ L of DMPO-benzyl alcohol solution (1 : 10, v/v) was added. The mixture was oscillated to obtain well-blending suspension. The irradiation source ($\lambda > 420$ nm) was a 300 W Xe arc lamp system, the very light source for our photocatalytic selective oxidation of alcohols. The settings for the ESR spectrometer were as follows: center field = 3512 G, microwave frequency = 9.86 GHz, and power = 6.35 mW. The photoelectrochemical analysis was conducted in a homemade three electrode cell. A Pt plate was employed as the counter electrode and an Ag/AgCl electrode was used as the reference electrode. The electrolyte was 0.2 M Na₂SO₄ aqueous solution without additive (pH 6.8). The working electrode was prepared on fluorine doped tin oxide (FTO) glass that was sonicated in ethanol and dried at 80 °C before use. The boundary of FTO glass was protected using Scotch tape. The 2 mg sample was adequately dispersed in 0.5 mL of *N,N*-dimethylformamide with sonication. The as-obtained slurry was spread onto the pre-treated FTO glass. After air drying, the working electrode was further dried at 120 °C for 2 h to improve adhesion. Then, the

Scotch tape was unstuck, and the uncoated part of the electrode was isolated with epoxy resin. The visible light irradiation source was a 300 W Xe arc lamp system equipped with a UV-CUT filter ($\lambda > 420$ nm). The electrochemical impedance spectroscopy (EIS) experiments and cyclic voltammograms were conducted on a CHI660D workstation (CH instrument, USA) in the electrolyte of 0.5 M KCl aqueous solution containing 0.01 M $K_3[Fe(CN)_6]$ - $K_4[Fe(CN)_6]$ (1 : 1) under open circuit potential conditions.

Catalytic activity

Photocatalytic selective oxidation of a range of alcohols was conducted according to the previous works.^{10,32,33,58–60} Typically, 0.1 mmol of alcohol and 8 mg of the as-synthesized catalyst were suspended in 1.5 mL of benzotrifluoride (BTF), which was saturated with molecular oxygen. Subsequently, the above mixture was transferred into a 10 mL Pyrex glass bottle, which was filled with molecular oxygen at a pressure of 0.1 MPa and stirred for 20 min to establish the adsorption-desorption equilibrium. The mixture was irradiated by a 300 W Xe arc lamp (PLS-SXE 300, Beijing Perfect light Co., Ltd.) with a UV-CUT filter to cut off light of wavelength less than 420 nm. After that, the mixture was centrifuged at 12 000 rpm for 10 min to remove the catalyst particles. The remaining solution was analyzed using an Agilent gas chromatograph (GC-7820). Conversion of alcohol, yield and selectivity for aldehyde were defined as follows:

$$\text{Conversion (\%)} = [(C_0 - C_r)/C_0] \times 100$$

$$\text{Yield (\%)} = C_p/C_0 \times 100$$

$$\text{Selectivity (\%)} = [C_p/(C_0 - C_r)] \times 100$$

where C_0 is the initial concentration of alcohol and C_r and C_p are the concentrations of the substrate alcohol and the corresponding product aldehyde, respectively, at a certain time after the photocatalytic reaction.

Results and discussion

The synthesis of blank In_2S_3 and In_2S_3 -GR nanocomposites with different weight addition ratios of GR is graphically



Scheme 1 The schematic illustration for the preparation of blank flowerlike In_2S_3 structure and In_2S_3 -GR nanocomposites *via* a facile, *in situ* hydrothermal method.

portrayed in Scheme 1. For blank In_2S_3 , the functional groups in *L*-cysteine molecule, such as $-NH_2$, $-COOH$, and $-SH$ (Fig. S1†), are crucial for the formation of flowerlike In_2S_3 structure. Firstly, a complex is formed *via* the coordination between In^{3+} ions and *L*-cysteine due to their strong interactions.^{40,49} During the hydrothermal process, the complex is decomposed to form In_2S_3 nuclei, followed by crystal growth at the expense of the small crystals. With the evolution of the hydrothermal reaction, the flowerlike In_2S_3 structures are gradually assembled using *L*-cysteine as a sulfide source and grafting molecular.⁴⁹ As for the fabrication of In_2S_3 -GR nanocomposites, $In(NO_3)_3$ aqueous solution is firstly mixed with a certain amount of GO, during which In^{3+} ions primarily anchor on the surface of GO mat through electrostatic attractive interaction between them. In the process of the subsequent hydrothermal treatment, *L*-cysteine is decomposed to provide S^{2-} and simultaneously hierarchical petal-like In_2S_3 architectures grow on conductive GR sheets formed by the reduction of nonconductive GO. The efficient reduction of GO to GR after the hydrothermal process can be evidenced by the Fourier transformed infrared spectroscopy (FT-IR),^{35,61} as displayed in Fig. S2 (ESI†). According to the FT-IR spectra of the pristine GO, the stretching vibrations including O-H (3426 cm^{-1}), C=O (1720 cm^{-1}), C=C (1622 cm^{-1}), C-O-H (1408 cm^{-1}), C-OH (1224 cm^{-1}), and C-O-C (1057 cm^{-1}) are observed, indicating the existence of various oxygen-containing functional groups on the GO surface.^{35,57,61} For In_2S_3 -1%GR, the intensity of various oxygen-containing functional groups is significantly decreased, which manifests the efficient reduction of GO to GR after the hydrothermal treatment.

Typical SEM analysis is used to observe the morphology of blank In_2S_3 and In_2S_3 -GR nanocomposites. As shown in Fig. 1A, without addition of GO, flowerlike structures for blank In_2S_3 with the average diameter of 1 μm are obtained. Once GO is introduced, the morphology of flowerlike In_2S_3 structure changes dramatically. As displayed in Fig. 1B, when the weight addition ratio of GR is 0.1%, the flowerlike morphology of blank

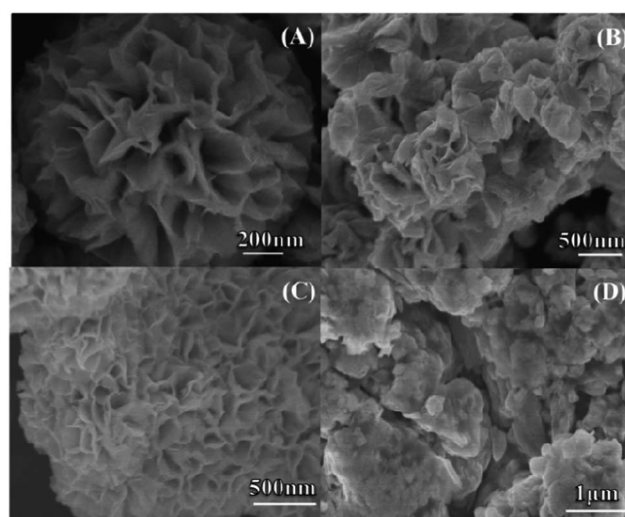


Fig. 1 Typical FESEM images of (A) blank In_2S_3 , (B) In_2S_3 -0.1%GR, (C) In_2S_3 -1%GR, and (D) In_2S_3 -2%GR.

In_2S_3 has been damaged apparently and petal-like In_2S_3 architectures start to grow along the 2D GR platform. With the further increase of GR to 1%, the compact hierarchical petal-like architectures of In_2S_3 grown onto the GR mat become more obvious (Fig. 1C). When the weight addition ratio of GR is increased to 2% (Fig. 1D), the petal-like architectures of In_2S_3 disappear, and the evident agglomeration of In_2S_3 particles occurs. The SEM results reveal that the addition of GO has a great influence on the morphology of the as-obtained In_2S_3 -GR nanocomposites, and the synthesis of In_2S_3 -GR with an appropriate amount of GO is a key factor for achieving different morphology of In_2S_3 spreading onto the 2D GR scaffold.

To further obtain the microscopic structure information of blank In_2S_3 and In_2S_3 -GR, transmission electron microscopy (TEM) analysis has been conducted as displayed in Fig. 2. It can be seen from Fig. 2A that without the addition of GO, flowerlike structure of blank In_2S_3 has been obtained. In comparison, with the addition of an appropriate amount of GO such as 1%, as shown in Fig. 2B and C, it is obvious to see that the hierarchical petal-like architectures of In_2S_3 are growing onto the GR mat compactly which ensures the good interfacial contact between In_2S_3 and GR. The results are in good accordance with the SEM analysis. The image of high resolution TEM (HRTEM) in Fig. 2D shows the distinct lattice fringe and the spacing is measured to be 0.324 nm, which is corresponding to the (311) planes of cubic β - In_2S_3 phase. The selected area electron diffraction (SAED) pattern indicates that the In_2S_3 -1%GR nanocomposite possesses polycrystalline structure, which is consistent with the following XRD results.

The XRD patterns in Fig. 3 exhibit the crystallographic structure and phase purity of the In_2S_3 -GR nanocomposites and

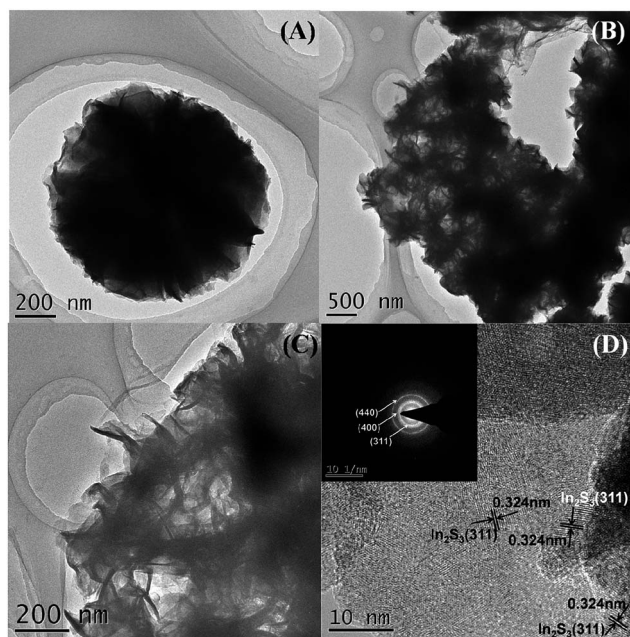


Fig. 2 TEM images of (A) blank In_2S_3 , (B) and (C) In_2S_3 -1%GR, and high-resolution TEM (HR-TEM) image of (D) In_2S_3 -1%GR; the inset of (D) is the image of SAED pattern of In_2S_3 -1%GR.

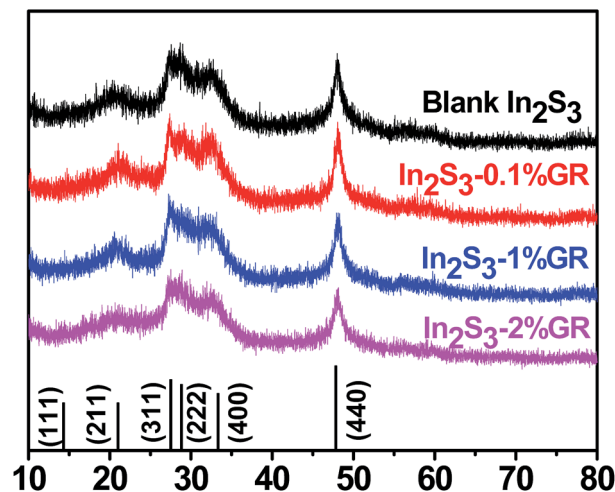


Fig. 3 The XRD spectra of the as-synthesized blank In_2S_3 and In_2S_3 -GR nanocomposites with different weight addition ratios of GR.

blank In_2S_3 . It can be seen that the In_2S_3 -GR nanocomposites with different weight ratios of GR display similar XRD patterns to that of blank In_2S_3 . The peaks located at *ca.* 14.2°, 20.9°, 27.4°, 28.7°, 33.2°, and 47.7° can be indexed to the (111), (211), (311), (222), (400), and (440) crystal planes for the cubic β - In_2S_3 phase (JCPDS no. 32-0456), respectively. No diffraction peaks of other crystal phases are observed, manifesting that the pure cubic β - In_2S_3 is formed during the current synthesis conditions. Notably, as compared to blank In_2S_3 , there are no apparent peaks for the separate GR in the In_2S_3 -GR nanocomposites to be detected, which can be probably ascribed to the relatively low addition amount of GR in the In_2S_3 -GR nanocomposites and the overlapping of the main characteristic peak of GR at 26.0° with the (311) peak at 27.4° for cubic β - In_2S_3 .^{10,32,33,58,62}

Fig. 4 displays the UV-vis diffuse reflectance spectra (DRS) for characterization of the optical properties of In_2S_3 -GR nanocomposites and blank In_2S_3 . It can be found that the addition of different amounts of GR has a great influence on the visible

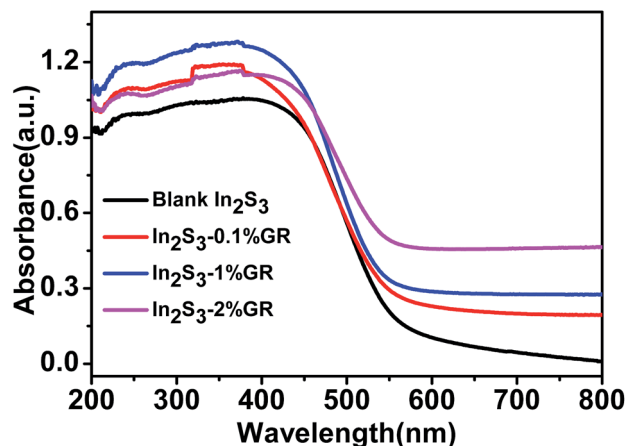


Fig. 4 The UV-vis DRS spectra of blank In_2S_3 and In_2S_3 -GR nanocomposites with different weight addition ratios of GR.

light absorption property of In_2S_3 -GR nanocomposites. With the increase of the weight addition ratios of GR, there is gradually enhanced absorption intensity in the visible light region of 560–800 nm, which should be ascribed to the intrinsic absorption of black colored GR. From the plot for the samples *via* the transformation based on the Kubelka–Munk function *versus* the energy of light, as shown in Fig. S3 (ESI†), the band gap values of the samples can be estimated to be *ca.* 2.54, 2.53, 2.49, and 2.46 eV, corresponding to blank In_2S_3 , In_2S_3 -0.1%GR, In_2S_3 -1%GR, and In_2S_3 -2%GR, respectively, indicating a band gap narrowing of the semiconductor In_2S_3 due to the introduction of GR into the matrix of In_2S_3 -GR nanocomposites. Such an extended optical absorption has also been observed in previous works regarding GR-semiconductor photocatalysts for solar-driven catalytic applications.^{21,27,28,63,64}

The photocatalytic performance of the In_2S_3 -GR nanocomposites is initially estimated by selective oxidation of benzyl alcohol to benzaldehyde under visible light irradiation ($\lambda > 420$ nm). It can be seen from Fig. 5 that the In_2S_3 -GR nanocomposites with different weight addition ratios of GR exhibit higher photoactivity than blank In_2S_3 toward selective oxidation of benzyl alcohol. Meanwhile, In_2S_3 -1%GR exhibits the highest photocatalytic activity, over which the conversion of benzyl alcohol is about 55% with high selectivity (*ca.* 99%) after the visible light irradiation for 2 h. When the weight addition ratio of GR reaches 2%, the photoactivity and selectivity are both reduced, which could be ascribed to the lowered contact surface of semiconductor In_2S_3 with the light irradiation in In_2S_3 -2% GR.^{21,33} Another reason for the decline in the selectivity is that the target product aldehyde may not be easily desorbed from the surface of photocatalyst due to the higher adsorption ability of carbon material GR with relatively higher addition in In_2S_3 -2% GR nanocomposite. Under this circumstance, further deep oxidation of aldehyde may occur, therefore resulting in the drop in selectivity.³³ As shown in Fig. 6, time-online profiles of

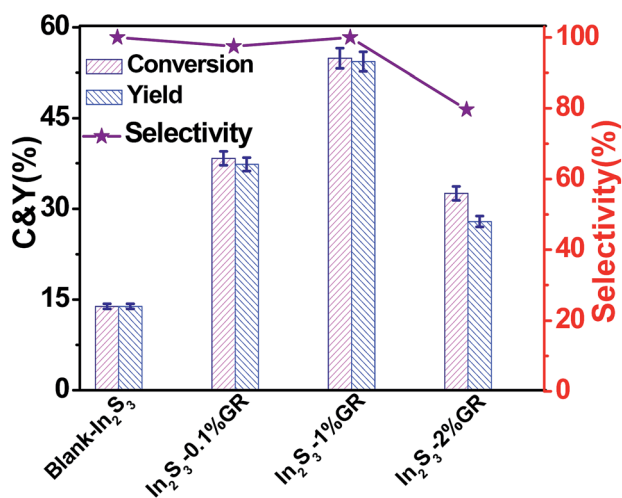


Fig. 5 Photocatalytic selective oxidation of benzyl alcohol to benzaldehyde over blank In_2S_3 and In_2S_3 -GR nanocomposites with different weight addition ratios of GR under visible light irradiation ($\lambda > 420$ nm) for 2 h.

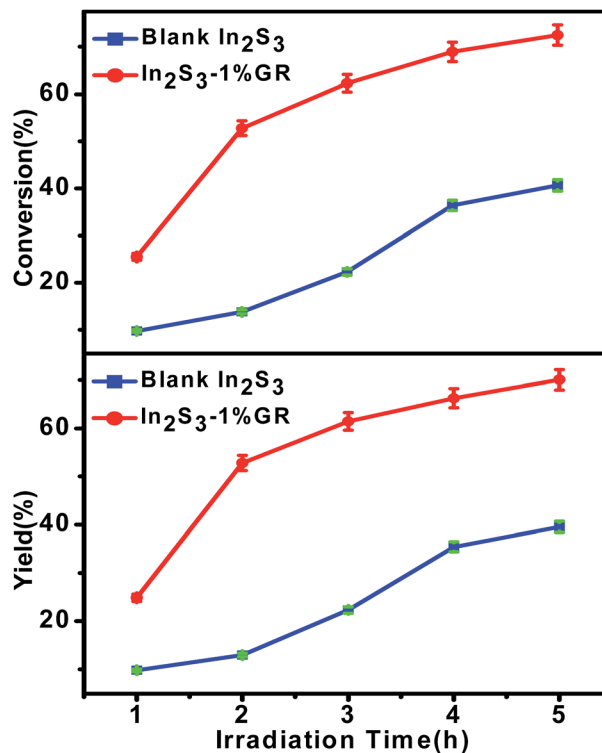


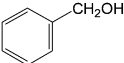
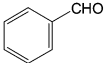
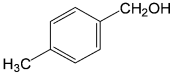
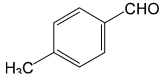
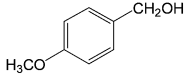
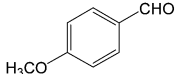
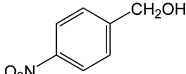
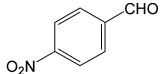
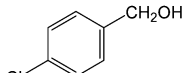
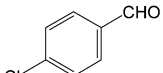
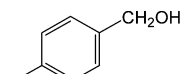
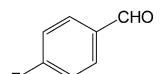
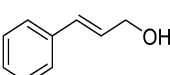
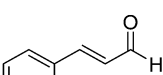
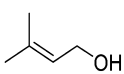
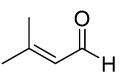
Fig. 6 Time-online photocatalytic selective oxidation of benzyl alcohol to benzaldehyde over the as-prepared blank In_2S_3 and In_2S_3 -1%GR under visible light irradiation ($\lambda > 420$ nm).

selective oxidation of benzyl alcohol over blank In_2S_3 and the optimal In_2S_3 -1%GR indicate that the conversion of benzyl alcohol and yield of benzaldehyde increase gradually with the irradiation time and the superior photoactivity of In_2S_3 -1%GR over blank In_2S_3 is obvious.

To further confirm the higher photoactivity of In_2S_3 -1%GR than blank In_2S_3 , we have also conducted the activity testing on oxidation of other benzylic alcohols and allylic alcohols under visible light irradiation. As demonstrated in Table 1, the In_2S_3 -1%GR nanocomposite exhibits higher photocatalytic activity than blank In_2S_3 in all selected reaction systems. Hence, it is clear that with the addition of appropriate amount of GR, the as-prepared In_2S_3 -1%GR shows remarkably enhanced photoactivity toward selective oxidation of a range of alcohols under visible light irradiation as compared to blank In_2S_3 .

To understand and explore the origins of the higher photoactivity of In_2S_3 -1%GR for selective oxidation of alcohols than blank In_2S_3 , a series of characterizations have been carried out. The transient photocurrent density of In_2S_3 -1%GR and blank In_2S_3 electrodes under visible light irradiation has shown in Fig. 7. It is clear to see that the photocurrent density of In_2S_3 -1%GR under visible light illumination is much higher than that of blank In_2S_3 . It is well known that the photocurrent is generated mainly by the diffusion of photo-induced electrons to the back contact, and at the same time, the photogenerated holes are taken up by the hole acceptor in the electrolyte.^{33,65} Therefore, the enhanced photocurrent over In_2S_3 -1%GR implies more efficient separation of photo-induced charge

Table 1 The photocatalytic performance of blank In_2S_3 and In_2S_3 -1%GR for selective oxidation of a range of alcohols under visible light irradiation ($\lambda > 420$ nm) for 2 h

| Entry | Substrate | Product | Time (h) | Blank In_2S_3 | | In_2S_3 -1%GR | |
|-------|--|--|----------|-------------------------------|-----------|-------------------------------|-----------|
| | | | | Conv. (%) | Yield (%) | Conv. (%) | Yield (%) |
| 1 |  |  | 2 | 14 | 14 | 55 | 54 |
| 2 |  |  | 2 | 18 | 15 | 32 | 30 |
| 3 |  |  | 2 | 43 | 39 | 56 | 56 |
| 4 |  |  | 2 | 10 | 9 | 20 | 20 |
| 5 |  |  | 2 | 24 | 23 | 50 | 49 |
| 6 |  |  | 2 | 14 | 14 | 31 | 29 |
| 7 |  |  | 2 | 10 | 7 | 18 | 15 |
| 8 |  |  | 2 | 14 | 12 | 25 | 25 |

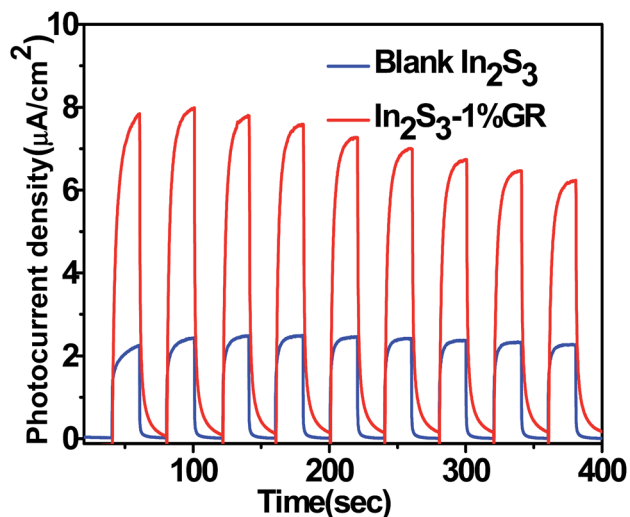


Fig. 7 Transient photocurrent density of as-prepared blank In_2S_3 and In_2S_3 -1%GR electrodes in the electrolyte of 0.2 M Na_2SO_4 aqueous solution without bias versus Ag/AgCl under visible light irradiation ($\lambda > 420$ nm).

carriers and longer lifetime of the photogenerated electron-hole pairs as compared with blank In_2S_3 , which can be ascribed to the introduction of conductive GR and the good interfacial

contact between In_2S_3 and GR. This can be further confirmed by the photoluminescence (PL) spectra measurements. The PL spectra give the information about photoexcited energy/electron transfer and recombination processes.^{33,36,66-68} As

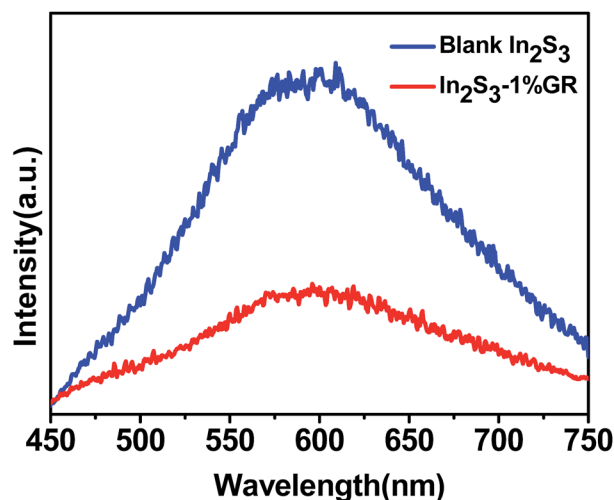


Fig. 8 Photoluminescence (PL) spectra of blank In_2S_3 and In_2S_3 -1%GR with an excitation wavelength of 420 nm.

displayed in Fig. 8, the PL intensity observed for In_2S_3 -1%GR is weaker than that of blank In_2S_3 with the excitation wavelength of 420 nm, thus indicating the more effective inhibition of the recombination of photogenerated charge carriers over In_2S_3 -1%GR than blank In_2S_3 .

Additionally, electrochemical impedance spectroscopy (EIS) has been performed to study the migration of charge carriers in the electrode materials.⁶⁹ From the EIS Nyquist plots of blank In_2S_3 and In_2S_3 -1%GR electrode materials cycled in 0.5 M KCl aqueous solution containing 0.01 M $\text{K}_3[\text{Fe}(\text{CN})_6]$ - $\text{K}_4[\text{Fe}(\text{CN})_6]$ (1 : 1) electrolyte solution (Fig. 9), we can see that both of the samples show semicircles at high frequencies. Under the similar preparation of the electrodes and electrolyte, the high-frequency arc corresponds to the charge transfer limiting process and can be attributed to the charge transfer resistance at the contact interface between the electrode and electrolyte solution.^{33,35,58,61} The smaller arc of In_2S_3 -1%GR than that of blank In_2S_3 indicates that the In_2S_3 -1%GR photocatalyst has faster interfacial electron transfer than blank In_2S_3 .

Furthermore, to understand the role of GR on affecting the surface area and pore structure of the samples, the Brunauer-Emmett-Teller (BET) surface area and porosity for In_2S_3 -1%GR and blank In_2S_3 have also been investigated. It can be found from Fig. 10 that both of the In_2S_3 -1%GR and blank In_2S_3 exhibit type IV isotherm with a typical H3 hysteresis loop characteristic of mesoporous solids according to the IUPAC classification.^{62,70} As illustrated in Table S1 (ESI[†]), the specific surface area and pore volume for In_2S_3 -1%GR are measured to be *ca.* $37 \text{ m}^2 \text{ g}^{-1}$ and $0.23 \text{ cm}^3 \text{ g}^{-1}$, respectively, which are larger than those for blank In_2S_3 (*ca.* $18 \text{ m}^2 \text{ g}^{-1}$ and $0.11 \text{ cm}^3 \text{ g}^{-1}$). Besides, adsorption experiments in the dark for various alcohols have been conducted (Fig. S4, ESI[†]). The results indicate that the In_2S_3 -1%GR with larger surface area shows enhanced adsorptivity toward various alcohols than blank In_2S_3 , which is favorable to promote the photoactivity.¹⁰⁻¹²

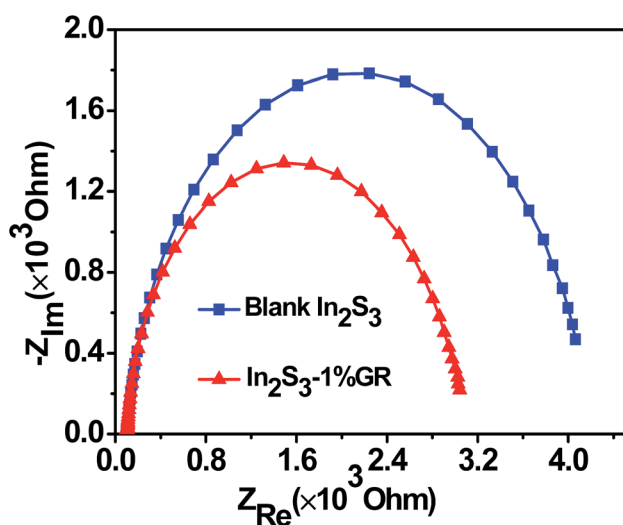


Fig. 9 Nyquist impedance plots of blank In_2S_3 and In_2S_3 -1%GR electrodes in 0.5 M KCl aqueous solution containing 0.01 M $\text{K}_3[\text{Fe}(\text{CN})_6]$ - $\text{K}_4[\text{Fe}(\text{CN})_6]$ (1 : 1).

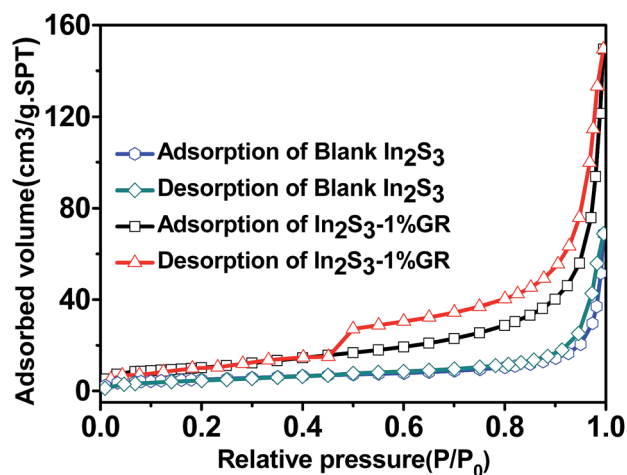


Fig. 10 Nitrogen adsorption-desorption isotherms of blank In_2S_3 and In_2S_3 -1%GR.

To investigate the possible mechanism for the photocatalytic performances over the samples, controlled experiments with addition of various radical scavengers for the photocatalytic selective oxidation of benzyl alcohol over blank In_2S_3 and In_2S_3 -1%GR in the BTF solvent have been carried out.^{32,71,72} The results displayed in Fig. 11 suggest that the primary active radical species are photogenerated holes, electrons and activated oxygen (*e.g.*, $\text{O}_2^{\cdot -}$), which can be also evidenced by the ESR spectra displayed in Fig. S5 (ESI[†]), as reflected by the decreased photoactivity obtained with the addition of AO, BQ, and $\text{K}_2\text{S}_2\text{O}_8$ as scavenger of photogenerated holes, superoxide radicals, and photogenerated electrons, respectively. Notably, although the photogenerated electrons can not directly participate in the

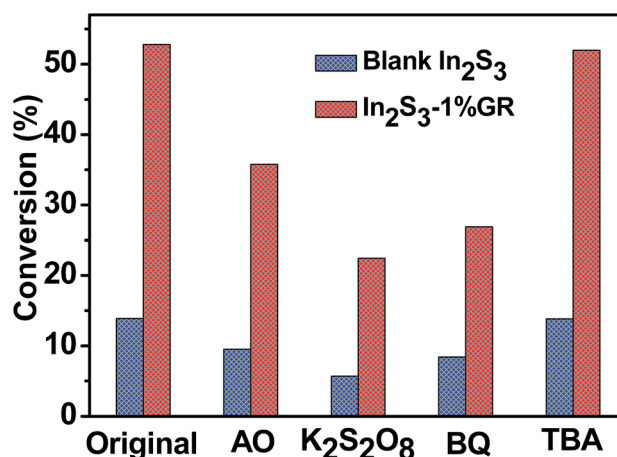


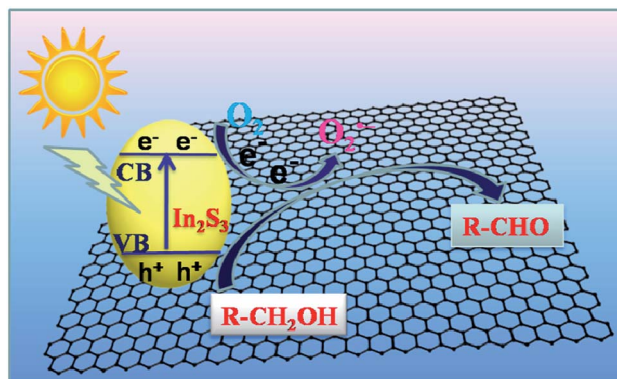
Fig. 11 Controlled experiments using different radical scavengers for the photocatalytic selective oxidation of benzyl alcohol over blank In_2S_3 and In_2S_3 -1%GR in the BTF solvent under visible light irradiation ($\lambda > 420 \text{ nm}$) for 2 h; ammonium oxalate (AO) is scavenger for photogenerated holes, $\text{K}_2\text{S}_2\text{O}_8$ for photogenerated electrons, benzoquinone (BQ) for superoxide radicals and *tert*-butyl alcohol (TBA) for hydroxyl radicals.

oxidation reaction, they can activate molecular oxygen. Thus, we can observe the decrease of conversion when the scavenger $K_2S_2O_8$ for photogenerated electrons is added into the reaction system. The addition of TBA as scavenger for hydroxyl radicals has almost no influence on the photoactivity of blank In_2S_3 and In_2S_3 -1%GR. This is reasonable because there are no strong and nonselective hydroxyl radicals present in the BTF solvent system.^{10,32,33,73}

The photostability of In_2S_3 -1%GR has also been investigated, as shown in Fig. 12. In_2S_3 -1%GR has the excellent recycled performance in four successive recycling tests toward photocatalytic selective oxidation of benzyl alcohol in the organic solvent of BTF under visible light. After four recycles, the In_2S_3 -1%GR nanocomposite shows almost no deactivation, suggesting that In_2S_3 -1%GR can serve as a stable visible light responsive photocatalyst toward selective oxidation of alcohols in our reaction conditions.

Based on the above discussions, the remarkable enhancement of photoactivity for In_2S_3 -GR nanocomposites over blank In_2S_3 can be attributed to the efficient separation and transfer efficiency of photogenerated electron-hole pairs and the larger surface area.

Scheme 2 shows the possible mechanism in which the electrons are firstly excited from the valence band (VB) to the conduction band (CB) (-0.8 V vs. NHE) of In_2S_3 in the In_2S_3 -GR nanocomposites, leaving holes in the VB. Then, photogenerated electrons can transfer to GR sheets (its work function is -0.08 V vs. NHE). Due to the good interfacial contact between In_2S_3 and GR, the photoexcited electrons can readily transfer to GR, which efficiently hampers the recombination of electrons and holes. The adsorbed alcohol can be oxidized by the hole to form alcohol radical cation, reacting with molecular oxygen or superoxide radicals to produce target aldehyde.⁷⁴



Scheme 2 Schematic diagram of the charge carriers transfer and proposed mechanism for selective oxidation of alcohols to corresponding aldehydes over the In_2S_3 -GR nanocomposites under visible light irradiation ($\lambda > 420$ nm).

Conclusions

In summary, we have successfully fabricated In_2S_3 -graphene (GR) nanocomposites with hierarchical petal-like In_2S_3 over-spreading the GR sheets. In virtue of the “structure directing” role of graphene oxide (GO) as the precursor of GR, the as-synthesized In_2S_3 -GR featuring the good interfacial contact between In_2S_3 and GR exhibit much higher photocatalytic activity toward selective oxidation of alcohols to aldehydes under visible light irradiation than blank flowerlike In_2S_3 . It is revealed that the significantly enhanced photocatalytic performance of In_2S_3 -GR is ascribed to the integrative effect of the boosted separation and transfer efficiency of photogenerated electron-hole pairs and the larger surface area. Our work highlights the promising scope of fabricating GR-based semiconductor nanocomposites with controllable architectural nanostructures by rationally utilizing the “structure directing” property of GO and extending their applications toward photocatalytic selective transformations.

Acknowledgements

The support by the National Natural Science Foundation of China (NSFC) (20903023, 21173045), the Award Program for Minjiang Scholar Professorship, the Natural Science Foundation (NSF) of Fujian Province for Distinguished Young Investigator Grant (2012J06003), and Program for Returned High-Level Overseas Chinese Scholars of Fujian province is gratefully acknowledged.

Notes and references

- 1 K. S. Novoselov, A. K. Geim, S. V. Morozov, D. Jiang, Y. Zhang, S. V. Dubonos, I. V. Grigorieva and A. A. Firsov, *Science*, 2004, **306**, 666–669.
- 2 N. Zhang, Y. Zhang and Y.-J. Xu, *Nanoscale*, 2012, **4**, 5792–5813.

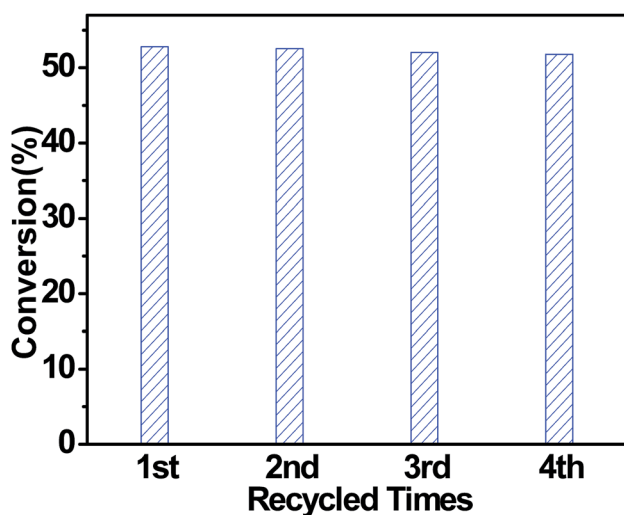


Fig. 12 Recycled testing of In_2S_3 -1%GR toward selective oxidation of benzyl alcohol under visible light irradiation ($\lambda > 420$ nm) for 2 h.

- 3 G. Xie, K. Zhang, B. Guo, Q. Liu, L. Fang and J. R. Gong, *Adv. Mater.*, 2013, **25**, 3820–3839.
- 4 C. Han, M.-Q. Yang, N. Zhang and Y.-J. Xu, *J. Mater. Chem. A*, 2014, **2**, 19156–19166.
- 5 M. Zhu, P. Chen and M. Liu, *ACS Nano*, 2011, **5**, 4529–4536.
- 6 Q. Zhang, C. Tian, A. Wu, T. Tan, L. Sun, L. Wang and H. Fu, *J. Mater. Chem.*, 2012, **22**, 11778–11784.
- 7 J. Zhang, J. Yu, M. Jaroniec and J. R. Gong, *Nano Lett.*, 2012, **12**, 4584–4589.
- 8 W. Tu, Y. Zhou, Q. Liu, Z. Tian, J. Gao, X. Chen, H. Zhang, J. Liu and Z. Zou, *Adv. Funct. Mater.*, 2012, **22**, 1215–1221.
- 9 A. Iwase, Y. H. Ng, Y. Ishiguro, A. Kudo and R. Amal, *J. Am. Chem. Soc.*, 2011, **133**, 11054–11057.
- 10 Y. Zhang, Z.-R. Tang, X. Fu and Y.-J. Xu, *ACS Nano*, 2011, **5**, 7426–7435.
- 11 C. Han, M.-Q. Yang, B. Weng and Y.-J. Xu, *Phys. Chem. Chem. Phys.*, 2014, **16**, 16891–16903.
- 12 M.-Q. Yang, N. Zhang, M. Pagliaro and Y.-J. Xu, *Chem. Soc. Rev.*, 2014, **43**, 8240–8254.
- 13 Q. Xiang, J. Yu and M. Jaroniec, *Chem. Soc. Rev.*, 2012, **41**, 782–796.
- 14 I. V. Lightcap and P. V. Kamat, *Acc. Chem. Res.*, 2012, **46**, 2235–2243.
- 15 L. Han, P. Wang and S. Dong, *Nanoscale*, 2012, **4**, 5814–5825.
- 16 W. Fan, Q. Zhang and Y. Wang, *Phys. Chem. Chem. Phys.*, 2013, **15**, 2632–2649.
- 17 O. Akhavan and E. Ghaderi, *J. Phys. Chem. C*, 2009, **113**, 20214–20220.
- 18 P. Gao, J. Liu, S. Lee, T. Zhang and D. D. Sun, *J. Mater. Chem.*, 2012, **22**, 2292–2298.
- 19 W. Fan, Q. Lai, Q. Zhang and Y. Wang, *J. Phys. Chem. C*, 2011, **115**, 10694–10701.
- 20 J. Zhou, G. Tian, Y. Chen, X. Meng, Y. Shi, X. Cao, K. Pan and H. Fu, *Chem. Commun.*, 2013, **49**, 2237–2239.
- 21 Y. Zhang, Z.-R. Tang, X. Fu and Y.-J. Xu, *ACS Nano*, 2010, **4**, 7303–7314.
- 22 J. Zhang, Z. Xiong and X. Zhao, *J. Mater. Chem.*, 2011, **21**, 3634–3640.
- 23 Y. H. Ng, A. Iwase, A. Kudo and R. Amal, *J. Phys. Chem. Lett.*, 2010, **1**, 2607–2612.
- 24 I. Y. Kim, J. M. Lee, T. W. Kim, H. N. Kim, H. i. Kim, W. Choi and S. J. Hwang, *Small*, 2012, **8**, 1038–1048.
- 25 A. Mukherji, B. Seger, G. Q. Lu and L. Wang, *ACS Nano*, 2011, **5**, 3483–3492.
- 26 J. Du, X. Lai, N. Yang, J. Zhai, D. Kisailus, F. Su, D. Wang and L. Jiang, *ACS Nano*, 2010, **5**, 590–596.
- 27 H. Zhang, X. Lv, Y. Li, Y. Wang and J. Li, *ACS Nano*, 2009, **4**, 380–386.
- 28 C. Chen, W. Cai, M. Long, B. Zhou, Y. Wu, D. Wu and Y. Feng, *ACS Nano*, 2010, **4**, 6425–6432.
- 29 E. Gao, W. Wang, M. Shang and J. Xu, *Phys. Chem. Chem. Phys.*, 2011, **13**, 2887–2893.
- 30 Y. Fu, P. Xiong, H. Chen, X. Sun and X. Wang, *Ind. Eng. Chem. Res.*, 2012, **51**, 725–731.
- 31 X. An, X. Yu, C. Y. Jimmy and G. Zhang, *J. Mater. Chem. A*, 2013, **1**, 5158–5164.
- 32 N. Zhang, M.-Q. Yang, Z.-R. Tang and Y.-J. Xu, *ACS Nano*, 2014, **8**, 623–633.
- 33 N. Zhang, Y. Zhang, X. Pan, X. Fu, S. Liu and Y.-J. Xu, *J. Phys. Chem. C*, 2011, **115**, 23501–23511.
- 34 M.-Q. Yang and Y.-J. Xu, *Phys. Chem. Chem. Phys.*, 2013, **15**, 19102–19118.
- 35 S. Liu, Z. Chen, N. Zhang, Z.-R. Tang and Y.-J. Xu, *J. Phys. Chem. C*, 2013, **117**, 8251–8261.
- 36 M.-Q. Yang, B. Weng and Y.-J. Xu, *Langmuir*, 2013, **29**, 10549–10558.
- 37 Y. HeeáKim, J. HakáLee, S. MináPark, J. SooáMoon and J. GyuáNam, *Chem. Commun.*, 2010, **46**, 2292–2294.
- 38 S. Rengaraj, S. Venkataraj, C.-w. Tai, Y. Kim, E. Repo and M. Sillanpää, *Langmuir*, 2011, **27**, 5534–5541.
- 39 W. Qiu, M. Xu, X. Yang, F. Chen, Y. Nan, J. Zhang, H. Iwai and H. Chen, *J. Mater. Chem.*, 2011, **21**, 13327–13333.
- 40 L.-Y. Chen, Z.-D. Zhang and W.-Z. Wang, *J. Phys. Chem. C*, 2008, **112**, 4117–4123.
- 41 K. H. Park, K. Jang and S. U. Son, *Angew. Chem., Int. Ed.*, 2006, **45**, 4608–4612.
- 42 B. Pejova and I. Bineva, *J. Phys. Chem. C*, 2013, **117**, 7303–7314.
- 43 Y. Gu and Y. Wang, *RSC Adv.*, 2014, **4**, 8582–8589.
- 44 F. Ye, G. Du, Z. Jiang, Y. Zhong, X. Wang, Q. Cao and J. Z. Jiang, *Nanoscale*, 2012, **4**, 7354–7357.
- 45 W. Du, J. Zhu, S. Li and X. Qian, *Cryst. Growth Des.*, 2008, **8**, 2130–2136.
- 46 F. Ye, C. Wang, G. Du, X. Chen, Y. Zhong and J. Jiang, *J. Mater. Chem.*, 2011, **21**, 17063–17065.
- 47 L. Liu, H. Liu, H.-Z. Kou, Y. Wang, Z. Zhou, M. Ren, M. Ge and X. He, *Cryst. Growth Des.*, 2008, **9**, 113–117.
- 48 Y. He, D. Li, G. Xiao, W. Chen, Y. Chen, M. Sun, H. Huang and X. Fu, *J. Phys. Chem. C*, 2009, **113**, 5254–5262.
- 49 X. An, J. C. Yu, F. Wang, C. Li and Y. Li, *Appl. Catal., B*, 2013, **129**, 80–88.
- 50 W. S. Hummers and R. E. Offeman, *J. Am. Chem. Soc.*, 1958, **80**, 1339.
- 51 N. I. Kovtyukhova, P. J. Ollivier, B. R. Martin, T. E. Mallouk, S. A. Chizhik, E. V. Buzaneva and A. D. Gorchinskiy, *Chem. Mater.*, 1999, **11**, 771–778.
- 52 L. J. Cote, F. Kim and J. Huang, *J. Am. Chem. Soc.*, 2008, **131**, 1043–1049.
- 53 D. Pan, S. Wang, B. Zhao, M. Wu, H. Zhang, Y. Wang and Z. Jiao, *Chem. Mater.*, 2009, **21**, 3136–3142.
- 54 D. Li, M. B. Müller, S. Gilje, R. B. Kaner and G. G. Wallace, *Nat. Nanotechnol.*, 2008, **3**, 101–105.
- 55 L. J. Cote, F. Kim and J. Huang, *J. Am. Chem. Soc.*, 2008, **131**, 1043–1049.
- 56 Y. Zhang, N. Zhang, Z.-R. Tang and Y.-J. Xu, *J. Phys. Chem. C*, 2014, **118**, 5299–5308.
- 57 Y. Zhang, N. Zhang, Z.-R. Tang and Y.-J. Xu, *ACS Nano*, 2012, **6**, 9777–9789.
- 58 N. Zhang, Y. Zhang, X. Pan, M.-Q. Yang and Y.-J. Xu, *J. Phys. Chem. C*, 2012, **116**, 18023–18031.
- 59 M. Zhang, C. Chen, W. Ma and J. Zhao, *Angew. Chem., Int. Ed.*, 2008, **47**, 9730–9733.

- 60 M. Zhang, Q. Wang, C. Chen, L. Zang, W. Ma and J. Zhao, *Angew. Chem., Int. Ed.*, 2009, **48**, 6081–6084.
- 61 Z. Chen, S. Liu, M.-Q. Yang and Y.-J. Xu, *ACS Appl. Mater. Interfaces*, 2013, **5**, 4309–4319.
- 62 N. Zhang, Y. Zhang, M.-Q. Yang, Z.-R. Tang and Y.-J. Xu, *J. Catal.*, 2013, **299**, 210–221.
- 63 Y.-J. Xu, Y. Zhuang and X. Fu, *J. Phys. Chem. C*, 2010, **114**, 2669–2676.
- 64 X.-Y. Zhang, H.-P. Li, X.-L. Cui and Y. Lin, *J. Mater. Chem.*, 2010, **20**, 2801–2806.
- 65 S. Soedergren, A. Hagfeldt, J. Olsson and S.-E. Lindquist, *J. Phys. Chem.*, 1994, **98**, 5552–5556.
- 66 J. Yang, H. Yan, X. Wang, F. Wen, Z. Wang, D. Fan, J. Shi and C. Li, *J. Catal.*, 2012, **290**, 151–157.
- 67 A. Cao, Z. Liu, S. Chu, M. Wu, Z. Ye, Z. Cai, Y. Chang, S. Wang, Q. Gong and Y. Liu, *Adv. Mater.*, 2010, **22**, 103–106.
- 68 M.-Q. Yang, B. Weng and Y.-J. Xu, *J. Mater. Chem. A*, 2014, **2**, 1710–1720.
- 69 T. Lu, Y. Zhang, H. Li, L. Pan, Y. Li and Z. Sun, *Electrochim. Acta*, 2010, **55**, 4170–4173.
- 70 R. Pierotti and J. Rouquerol, *Pure Appl. Chem.*, 1985, **57**, 603–619.
- 71 Y. Zhang, N. Zhang, Z.-R. Tang and Y.-J. Xu, *Chem. Sci.*, 2013, **4**, 1820–1824.
- 72 Y. Zhang, N. Zhang, Z.-R. Tang and Y.-J. Xu, *Chem. Sci.*, 2012, **3**, 2812–2822.
- 73 Q. Wang, M. Zhang, C. Chen, W. Ma and J. Zhao, *Angew. Chem., Int. Ed.*, 2010, **49**, 7976–7979.
- 74 N. Zhang, X. Fu and Y.-J. Xu, *J. Mater. Chem.*, 2011, **21**, 8152–8158.